Journal of Magnetic Resonance **148,** 314–326 (2001)
doi:10.1006/jmre.2000.2253, available online at http://www.idealibrary.com on IDEAL®

# Signal-to-Noise Ratio Comparison of Encoding Methods for Hyperpolarized Noble Gas MRI

Lei Zhao, Arvind K. Venkatesh, Mitchell S. Albert, and Lawrence P. Panych

*Department of Radiology, Harvard Medical School and Brigham and Women's Hospital, 75 Francis Street, Boston, Massachusetts 02115*

Received June 26, 2000; revised November 1, 2000

**Some non-Fourier encoding methods such as wavelet and direct encoding use spatially localized bases. The spatial localization feature of these methods enables optimized encoding for improved spatial and temporal resolution during dynamically adaptive MR imaging. These spatially localized bases, however, have inherently reduced image signal-to-noise ratio compared with Fourier or Hadamad encoding for proton imaging. Hyperpolarized noble gases, on the other hand, have quite different MR properties compared to proton, primarily the nonrenewability of the signal. It could be expected, therefore, that the characteristics of image SNR with respect to encoding method will also be very different from hyperpolarized noble gas MRI compared to proton MRI. In this article, hyperpolarized noble gas image SNRs of different encoding methods are compared theoretically using a matrix description of the encoding process. It is shown that image SNR for hyperpolarized noble gas imaging is maximized for any orthonormal encoding method. Methods are then proposed for designing RF pulses to achieve normalized encoding profiles using Fourier, Hadamard, wavelet, and direct encoding methods for hyperpolarized noble gases. Theoretical results are confirmed with hyperpolarized noble gas MRI experiments.** 

*Key Words:* **non-Fourier encoded MRI; signal-to-noise ratio; hyperpolarized noble gas MRI; spatially selective RF excitation; wavelet encoding.**

## 1. INTRODUCTION

With spatially selective RF excitation, non-Fourier encoding methods such as Hadamard, wavelet, and direct encoding can be implemented for magnetic resonance imaging (MRI). These non-Fourier encoding methods, especially those with spatially localized basis functions, can be used for adaptive imaging where the data acquisition strategy is modified according to information obtained during imaging (*1*). With adaptively optimized encoding bases, data acquisition redundancy can be reduced, thus improving temporal and spatial resolution during dynamic imaging.

Unfortunately, in proton MRI, the spatially localized bases that are especially useful for adaptive imaging, such as wavelet and direct encoding, give a significantly reduced image signal-to-noise ratio (SNR) compared with Fourier or Hadamard encoding. For example, the SNRs of wavelet and direct encoding were shown (*2*) to be $\sqrt{N/3}$ and $\sqrt{N}$, respectively, relative to the SNR of Fourier or Hadamard encoding, for an equal number of encoding steps, $N$. In Fourier or Hadamard encoding, all spins within the field-of-view (FOV) participate in each of the encoding steps, whereas in wavelet and direct encoding, not all of the spins contribute, resulting in a lower SNR. This reduced image SNR greatly limits the applications of these spatially localized non-Fourier encoding bases in proton MRI.

The SNR situation for hyperpolarized noble gas MRI (*3*) is quite different than for proton MRI. Because each RF excitation depletes some of the nonrenewable hyperpolarized magnetization, spatially localized encoding methods which use significantly fewer excitations within a given volume element, such as wavelet and direct encoding, cause much less depletion of the hyperpolarized magnetization. As a result, larger flip angles can be used on each RF excitation, thereby boosting image SNR. Thus, relative image SNRs for spatially localized encoding methods with hyperpolarized noble gas imaging differ from those for proton imaging.

In this paper, hyperpolarized noble gas image SNRs are analyzed theoretically using different orthogonal encoding bases. From this analysis, different encoding basis sets are optimized to produce maximal image SNR. The experimental results with optimized encoding bases are then compared with theoretical predictions.

## 2. THEORY

### 2.1. A Matrix Representation for MRI Encoding

In order to analyze image SNR and to optimize encoding bases, we adopt a matrix description of the encoding process, described elsewhere in detail (*4, 5*) and summarized here in brief. For simplicity, we will consider a 1-dimensional encoding model. The results for multidimensional magnetic resonance (MR) encoding techniques can be represented as separable 1D operations in multiple dimensions.

Let $s(x)$ represent a 1D MR signal density to be "imaged." Define $\Phi(x)$ as a function that is centered at $x = 0$ and has a spread of $\Delta x$, which will serve as a sampling or point-spread function of a pixel. We then define a spatially localized set of



1090-7807/01 $35.00

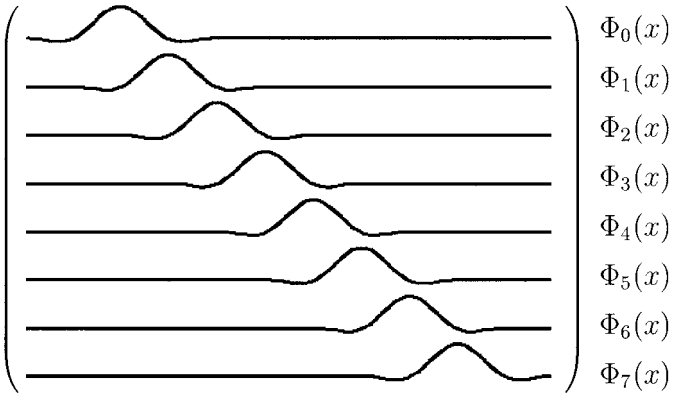


**FIG. 1.** A schematic diagram of a set of localized Battle–LeMarie-shape orthonormal functions.

orthonormal basis functions, $\{\Phi_m(x)\}$, that span the FOV along the spatial encoding direction $x$, such that

$$\Phi_m(x) = \Phi(x - m\Delta x) \quad m = 0, 1, \ldots, M-1,$$
$$\Delta x = \text{FOV}/M, \qquad [1]$$

where $M$ is the number of pixels along the FOV. A schematic diagram of a set of spatially localized orthonormal functions is shown in Fig. 1, where the point-spread function, $\Phi(x)$, is the Battle–LeMarie scaling function described in (*6*).

Since $\Phi_m(x)$ is the point-spread function of the imaging process and the set $\{\Phi_m(x)\}$ is orthogonal, $s(x)$ can be represented by the expansion

$$s(x) \cong \sum_m s_m \Phi_m(x), \qquad [2]$$

where

$$s_m = \int s^\dagger(x)\Phi_m(x)dx = \langle s(x), \Phi_m(x)\rangle. \qquad [3]$$

The set of $M$ reconstructed values $\{s_m\}$ represents a discrete estimate or "image" of $s(x)$. The approximation in Eq. [2] will be exact if $\{\Phi_m(x)\}$ is a complete basis.

In MR imaging, the encoding functions define the spatial distribution of the projection of spins on the transverse plane (the magnitudes and the precession angles of the spins) that one manipulates during the imaging experiment using a combination of gradient and RF pulses. These encoding functions $t_n(x)$ can be represented in terms of linear combinations of the basis functions in Eq. [1] such that

$$t_n(x) = \sum_{m=0}^{M-1} T_{nm}\Phi_m(x), \qquad [4]$$

where $T_{nm}$ is the element of an $N \times M$ encoding matrix $\bar{\bar{T}}$, and the encoding vectors are in the rows of $\bar{\bar{T}}$. For any orthogonal encoding matrix, $N$ is equal to $M$. In Fourier encoded MRI, each $t_n(x)$ is a complex exponential function and $\Phi(x)$ is a sinc-like function. In wavelet-encoding MRI, each $t_n(x)$ is a wavelet transform function, and $\Phi(x)$ is the "scaling function" of the wavelet basis (*2*, *7*).

The measured signal response $r_n$ from the $n$th encoding step will be

$$r_n = \langle s(x), t_n(x)\rangle = \langle s(x), \sum_{m=0}^{M-1} T_{nm}\Phi_m(x)\rangle$$
$$= \sum_{m=0}^{M-1} T_{nm}\langle s(x), \Phi_m(x)\rangle = \sum_{m=0}^{M-1} T_{nm}s_m, \qquad [5]$$

or

$$\bar{r} = \bar{\bar{T}}\bar{s}, \qquad [6]$$

where

$$\bar{r} = [r_0\ r_1 \ldots r_{N-1}]^T$$

and

$$\bar{s} = [s_0\ s_1 \ldots s_{M-1}]^T.$$

Therefore, a discrete 1D image estimate $\bar{s}$ can be reconstructed by

$$\bar{s} = \bar{\bar{T}}^{-1}\bar{r}. \qquad [7]$$

Here, we assume that $\bar{\bar{T}}$ is not singular, i.e., $\bar{\bar{T}}^{-1}$ exists. The rows of the encoding matrix $\bar{\bar{T}}$ for Fourier, wavelet, or Hadamard encoding can be obtained by the complex Fourier, wavelet, or Hadamard transform on the columns of the identity matrix. Thus, the encoding matrix $\bar{\bar{T}}$ is actually the same as the transform matrix operator of the Fourier, wavelet, or Hadamard transform. When $\bar{\bar{T}}$ is the identity matrix, it represents a direct spatial encoding, and no reconstruction is required. Two-dimensional imaging with direct spatial encoding along one dimension represents the case of direct encoding where individual lines of an image are obtained directly on each RF excitation. The encoding representation described above is illustrated in Fig. 2.

The point-spread function associated with a transform ma-

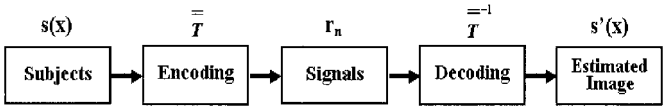


**FIG. 2.** Block diagram of MRI encoding representation.

trix is normally unique and is related to the transform. For example, the point-spread function associated with the Fourier transform is a sinc-like function. In this work, we use a generalized digital encoding approach developed by Panych *et al.* (*8*) to describe the encoding process. In such an approach, the point-spread function is made independent of the encoding basis. The generation of the encoding basis (a set of encoding functions) $\{t_n(x)\}$ is illustrated by Fig. 3, where the encoding matrix $\bar{\bar{T}}$ and the set of localized orthonormal point-spread functions $\Phi_m(x)$ are not necessarily related to each other.

### *2.2. SNR Analysis*

The MR signal measured, $\bar{r}'$, is a combination of the signal response defined in Eq. [6] and an additive random component, $\bar{\eta}$, representing the measurement noise vector,

$$\bar{r}' = \bar{r} + \bar{\eta} = \bar{\bar{T}}\bar{s} + \bar{\eta}. \qquad [8]$$

The reconstructed image $\bar{s}'$ is achieved by inverse transformation on $\bar{r}'$, which also transforms the measurement noise,

$$\begin{aligned} \bar{s}' &= \bar{\bar{T}}^{-1}\bar{r} + \bar{\bar{T}}^{-1}\bar{\eta}, \\ &= \bar{s} + \bar{\eta}', \end{aligned} \qquad [9]$$

where the elements of $\bar{s}$ are defined in Eq. [3], and $\bar{\eta}'$ is the image noise vector.

Image SNR is the square root of the ratio of the signal energy $E^{\mathrm{s}}$ to the noise energy $E^{\mathrm{n}}$,

$$\mathrm{SNR} = \sqrt{E^{\mathrm{s}}/E^{\mathrm{n}}}. \qquad [10]$$

For simplicity, we assume that all reconstruction methods are designed to produce images of the same signal level, so that the signal energy will be approximately the same for all encoding methods, and image SNR depends on the image noise energy only.

According to Eq. [9], the image noise energy is

$$E^{\mathrm{n}} = \epsilon[\bar{\eta}'^{\mathrm{T}}\bar{\eta}'] = \epsilon[(\bar{\bar{T}}^{-1}\bar{\eta})^{\mathrm{T}}(\bar{\bar{T}}^{-1}\bar{\eta})], \qquad [11]$$

where $\epsilon[x]$ represents the expectation of $x$. It has been shown (*2*) that, for all orthogonal encoding bases, the image noise energy can be represented as

$$E^{\mathrm{n}} = \sigma^2 \mathrm{Trace}[(\bar{\bar{T}}\bar{\bar{T}}^{T})^{-1}] = \sigma^2 \sum_{n=0}^{N-1} 1/\|t_n\|^2, \qquad [12]$$

where $\sigma^2 = \epsilon[\eta_i^2]$ and $\eta_i$ is the $i$th element of $\bar{\eta}$. Here, $\sigma^2$ is the variance of measurement noise which can be assumed constant for different encoding methods.

Based on our constant signal energy assumption, image SNRs of different encoding methods thus depend solely on $\|t_n\|^2$. According to Eq. [4],

$$\|t_n\|^2 = \sum_{m=0}^{M-1} T_{nm}^2. \qquad [13]$$

As discussed earlier, encoding functions define the spatial distribution of the projection of the transverse magnetization. Thus, in the ideal case when the point-spread function is box-shaped, $T_{nm}$ is proportional to the overall transverse magnetization, $P_{nm}^{[xy]}$, at pixel location $m$ immediately after the application of the $n$th encoding function and Eq. [13] becomes

$$\|t_n\|^2 = K \sum_{m=0}^{M-1} P_{nm}^{[xy]2}, \qquad [14]$$

where $K$ is a constant.

According to the Bloch equations (*9*), $P_{nm}^{[xy]}$ can be written as

$$\begin{aligned} P_{nm}^{[xy]} &= [P_{(n-1)m}^{[z]} e^{-\mathrm{TR}_{(n-1)m}/T_1(m)} \\ &\quad + P_m^{[00]}(1 - e^{-\mathrm{TR}_{(n-1)m}/T_1(m)})] \\ &\quad \times \sin\theta_n(m), \quad 1 \le n \le N-1, \\ P_{nm}^{[z]} &= P_{(n-1)m}^{[z]} \cos\theta_{(n-1)}(m) e^{-\mathrm{TR}_{(n-1)m}/T_1(m)} \\ &\quad + P_m^{[00]}(1 - e^{-\mathrm{TR}_{(n-1)m}/T_1(m)}), \quad 1 \le n \le N-1, \\ P_{0m}^{[xy]} &= P_m^{[00]} \sin\theta_0(m), \\ P_{0m}^{[z]} &= P_m^{[00]} \cos\theta_0(m), \end{aligned} \qquad [15]$$

where $P_{nm}^{[z]}$ represents the longitudinal magnetization at pixel location $m$ immediately after the application of the $n$th encoding function, $P_m^{[00]}$ is the initial longitudinal magnetization at pixel location $m$, $\mathrm{TR}_{nm}$ is the effective pulse repetition at pixel location $m$ between the $n$th and the $(n+1)$th encoding pulses, $\theta_n(m)$ is the $n$th RF pulse flip angle at the pixel location $m$, and $T_1(m)$ is the longitudinal relaxation time at pixel location $m$.

From Eqs. [10]–[15], it is seen that image SNR depends on the initial magnetization, longitudinal relaxation times, and how the magnetization is used with respect to choice of encoding pulse orders, RF pulse flip angles, and pulse repetition times. All of the above factors are necessary to compare image

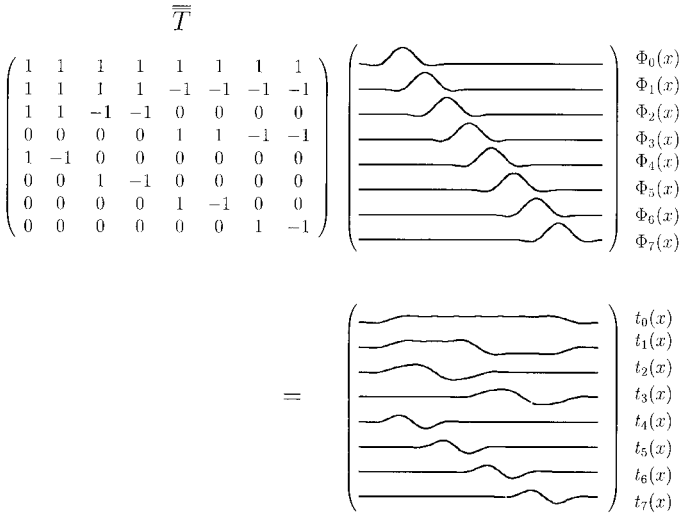


**FIG. 3.** Schematic description of the generation of encoding functions. The set of encoding functions $\{t_n(x)\}$ is represented by the linear combination of the set of point-spread functions according to the encoding matrix $\overline{\overline{T}}$.

SNRs of different encoding methods and it is not possible to derive a single equation that satisfies all conditions. To illustrate this issue, as an example, we will compare image SNRs of Fourier and direct encoding ($\overline{\overline{T}}$ = identity matrix) for three separate scenarios.

*Scenario I: Full longitudinal thermal magnetization recovery.* When TR $\gg T_1$, longitudinal magnetization is fully recovered between each TR. In such a case, a flip angle of $\pi/2$ can be used for both Fourier and direct encoding to maximize signal level. Given the same initial magnetization, the transverse magnetization level at each pixel after each RF pulse application will be the same using Fourier and direct encoding. To achieve an image resolution of $N$, $N$ excitations are required for both Fourier and direct encoding. While each pixel is excited $N$ times for Fourier encoding, however, only one excitation is applied to each pixel in direct encoding. According to Eqs. [12] and [14], the noise energy of Fourier encoding is $N$ times lower than that of direct encoding. Based on the equal signal energy assumption and Eq. [10], the SNR of Fourier encoding is $\sqrt{N}$ times higher than that of direct encoding, as demonstrated by Panych (*2*). This SNR gain of Fourier encoding results because there is full recovery of the longitudinal magnetization between excitations.

*Scenario II: Steady state.* When TR is comparable to $T_1$, the longitudinal magnetization does not fully recover between excitations resulting in a lower transverse magnetization than if longitudinal magnetization is fully recovered. The transverse magnetization level depends on the choice of RF pulse flip angle and, if the Ernst angle (*9*) is used, the transverse magnetization is maximized. In direct encoding, since each pixel is excited only once, the Ernst angle is $\pi/2$. Thus, the transverse magnetization remains the same as for full longitudinal magnetization recovery. For Fourier encoding, however, the transverse magnetization is usually significantly less than the transverse magnetization with full longitudinal magnetization recovery and, based on the analysis in Scenario I, the image SNR improvement using Fourier encoding will not be $\sqrt{N}$ times higher than for direct encoding. For example, for a $T_1$ of 800 ms and a pixel resolution of 128, the SNR improvement using Fourier encoding over direct encoding is 2.8, 4.0, 5.6, 7.7, 9.9, 11.2, and 11.3 for TRs of 100, 200, 400, 800, 1600, 4000, and 8000 ms, respectively. At the extreme case, when TR $\gg T_1$ (Scenario I), e.g., TR = 8000 ms and the Ernst angle is $\pi/2$, the SNR improvement of Fourier encoding over direct encoding is maximized at $\sqrt{128} = 11.3$.

*Scenario III: No longitudinal magnetization recovery.* When there is no longitudinal recovery, the transverse magnetization depends on the value of the initial magnetization and how this initial magnetization is used on each excitation.

There are two cases when magnetization recovery need not be considered. When TR $\ll T_1$, the thermal magnetization relaxation rate is too slow to be able to recover any significant longitudinal magnetization between each TR. Another case when longitudinal recovery can be ignored is for hyperpolarized noble gas imaging. Since the hyperpolarized magnetization (which never recovers) is up to five orders of magnitude higher than thermally polarized magnetization (which does recover), recovery of longitudinal magnetization is a minor factor contributing signal in hyperpolarized noble gas images.

When there is no recovery of the magnetization, the transverse magnetization is

$$\begin{aligned} P_{nm}^{[xy]} &= P_{(n-1)m}^{[z]} \sin\,\theta_n(m), \quad 1 \le n \le N-1, \\ P_{nm}^{[z]} &= P_{(n-1)m}^{[z]} \cos\,\theta_{(n-1)}(m), \quad 1 \le n \le N-1, \\ P_{0m}^{[xy]} &= P_m^{[00]} \sin\,\theta_0(m), \\ P_{0m}^{[z]} &= P_m^{[00]} \cos\,\theta_0(m). \end{aligned} \tag{16}$$

Thus,

$$\begin{aligned} \sum_{n=0}^{N-1} \|t_n\|^2 &= \sum_{n=0}^{N-1} \sum_{m=0}^{M-1} P_{nm}^{[xy]2} = \sum_{m=0}^{M-1} \sum_{n=0}^{N-1} P_{nm}^{[xy]2} \\ &= \sum_{m=0}^{M-1} [P_m^{[00]2} \sin^2\theta_0(m) \\ &\quad + P_m^{[00]2} \cos^2\theta_0(m) \sin^2\theta_1(m) + \cdots \\ &\quad + P_m^{[00]2} \cos^2\theta_0(m) \cdots \cos^2\theta_{N-3}(m) \\ &\quad \times \sin^2\theta_{N-2}(m) + P_m^{[00]2} \cos^2\theta_0(m) \cdots \\ &\quad \times \cos^2\theta_{N-3}(m) \cos^2\theta_{N-2}(m) \sin^2\theta_{N-1}(m)]. \end{aligned} \tag{17}$$

To effectively utilize the nonrenewable magnetization, one would expect to use a $\pi/2$ RF pulse for the last excitation. By plugging $\theta_{N-1}(m) = \pi/2$ into Eq. [17], we obtain

$$\sum_{n=0}^{N-1} \|t_n\|^2 = \sum_{m=0}^{M-1} P_m^{[00]2}, \qquad [18]$$

which is a constant for a given initial magnetization.

Equation [18] shows that when there is no recovery of the longitudinal magnetization and when there is no longitudinal magnetization remaining after the final excitation pulse, the total signal available for image encoding is equal to the total initial magnetization, which is the same for any encoding method.

Thus, for the case of imaging where there is no magnetization recovery, such as in hyperpolarized noble gas imaging, the problem of maximizing SNR can be stated such that, given a constant available magnetization (Eq. [18]), what is the restriction on each $\|t_n\|$ in order to minimize the image noise energy (Eq. [12])? As proven in the Appendix, when $\|t_i\|^2 = \|t_j\|^2 = \sum_{m=0}^{M-1} P_m^{[00]2}/N$, then $\Sigma\ 1/\|t_n\|^2$ is minimized. In other words, when $\overline{\overline{T}}$ is normalized, the noise energy, $E^n$, is minimized. Since, by definition, $E^s$ is the same for all encoding methods, we conclude that *for the case of imaging with no magnetization recovery, such as in hyperpolarized noble gas imaging, image SNR is maximized using any orthonormal encoding method.*

### *2.3. RF Pulse Design for Normalized Encoding Profiles*

It was shown in the previous section that, to achieve maximal image SNR for hyperpolarized noble gas imaging, an encoding basis must be normalized. The encoding functions of each basis define the spatial distribution of the projection of magnetization on the transverse plane, which is represented by the signal magnitudes and precession angles of the spins and is achieved by the application of RF pulses and gradients. Given a linear system assumption (which is valid for most encoding functions where the RF pulse flip angles are small) and a constant gradient, a certain spatial distribution of spin transverse magnetization (or encoding function profile) can be excited with an RF pulse that is simply designed using the Fourier transform of the encoding function.

In proton imaging, since the thermal magnetization can be recovered, the initial longitudinal magnetization can be assumed to be the same before each RF excitation (if the TR is long with respect to $T_1$). Thus, the flip angle of the spins in each pixel is proportional to the amplitude of the corresponding element of the encoding vector.

The case for hyperpolarized noble gas imaging is more complicated. Since the hyperpolarized magnetization is nonrenewable, the flip angle of the spins in each pixel has to be manipulated so that some longitudinal magnetization is preserved for subsequent excitations.

As shown in Fig. 3, for example, if the normalized encoding matrix is $\overline{\overline{T}}$, RF excitation pulses can be directly designed based on the function profiles of $\{t_n(x)\}$ for proton imaging. In hyperpolarized imaging, however, one has to adjust the amplitudes of the functions $\{t_n(x)\}$ to ensure a normalized spin excitation profile. We propose a scaling matrix $\overline{\overline{\Lambda}}$ to adjust the amplitudes of the elements in $\overline{\overline{T}}$ so that the RF pulses can be easily designed based on the scaled functions $\{t_n(x)\}$. In our method, $\overline{\overline{T}}$ is scaled by element-by-element multiplication with $\overline{\overline{\Lambda}}$. The elements on $\overline{\overline{\Lambda}}$ are determined by the number of excitations, the TR values at each pixel location, and $T_1$. The number of excitations and the TR values at each pixel location vary for different encoding bases.

*2.3.1. Fourier encoding.* As described previously, the encoding functions are expanded as linear combinations of the set of localized orthonormal basis functions (point-spread functions) defined in Eq. [1], where the combinations are represented by row vectors of the encoding matrix. In Fourier encoding, the encoding matrix is represented by the discrete Fourier transform matrix operator as shown in Eq. [19] for the case of $N = 8$.

$$\overline{\overline{F}} = \begin{bmatrix} 1 & 1 & 1 & 1 & 1 & 1 & 1 & 1 \\ 1 & e^{-i(\pi/4)} & e^{-i(\pi/2)} & e^{-i(3\pi/4)} & e^{i\pi} & e^{i(3\pi/4)} & e^{i(\pi/2)} & e^{i(\pi/4)} \\ 1 & e^{i(-\pi/2)} & e^{-i\pi} & e^{i(\pi/2)} & 1 & e^{-i(\pi/2)} & e^{-i\pi} & e^{i(\pi/2)} \\ 1 & e^{-i(3\pi/4)} & e^{i(\pi/2)} & e^{-i(\pi/4)} & e^{-i\pi} & e^{i(\pi/4)} & e^{-i(\pi/2)} & e^{i(3\pi/4)} \\ 1 & e^{i\pi} & 1 & e^{i\pi} & 1 & e^{i\pi} & 1 & e^{i\pi} \\ 1 & e^{i(3\pi/4)} & e^{-i(\pi/2)} & e^{i(\pi/4)} & e^{i\pi} & e^{-i(\pi/4)} & e^{i(\pi/2)} & e^{-i(3\pi/4)} \\ 1 & e^{i(\pi/2)} & e^{i\pi} & e^{-i(\pi/2)} & 1 & e^{i(\pi/2)} & e^{i\pi} & e^{-i(\pi/2)} \\ 1 & e^{i(\pi/4)} & e^{i(\pi/2)} & e^{i(3\pi/4)} & e^{-i\pi} & e^{-i(3\pi/4)} & e^{-i(\pi/2)} & e^{-i(\pi/4)} \end{bmatrix} \qquad [19]$$

In Fourier encoding, the spins along the FOV are excited with the same signal amplitude, but with a phase that varies linearly with position. Since all of the spins are excited on

every excitation, normalization of the encoding function matrix will not change the relative amplitude of each encoding function, i.e., the signal amplitude should be the same from excitation to excitation. To achieve such transverse magnetization distribution of spins for hyperpolarized noble gases, the variable-flip-angle technique, developed by Zhao *et al.* and described in (*10*), can be used to obtain the scaling matrix $\overline{\overline{\Lambda}}$. Equation [20] shows $\overline{\overline{\Lambda}}$ (in degrees) for the case of $N = 8$.

$$\overline{\overline{\Lambda}} = \begin{bmatrix} 21 & 21 & 21 & 21 & 21 & 21 & 21 & 21 \\ 22 & 22 & 22 & 22 & 22 & 22 & 22 & 22 \\ 24 & 24 & 24 & 24 & 24 & 24 & 24 & 24 \\ 27 & 27 & 27 & 27 & 27 & 27 & 27 & 27 \\ 30 & 30 & 30 & 30 & 30 & 30 & 30 & 30 \\ 35 & 35 & 35 & 35 & 35 & 35 & 35 & 35 \\ 45 & 45 & 45 & 45 & 45 & 45 & 45 & 45 \\ 90 & 90 & 90 & 90 & 90 & 90 & 90 & 90 \end{bmatrix} \quad [20]$$

The elements are the same along any row in the scaling matrix and the elements along each column correspond to those variable flip angles calculated in (*10*). A 90° pulse is used on the last excitation to utilize all of the remaining hyperpolarized magnetization.

*2.3.2. Hadamard encoding.* For Hadamard encoding, the Hadamard transform matrix operator is used to generate encoding functions. Equation [21] shows an eight-level Hadamard encoding matrix

$$\overline{\overline{H}} = \begin{bmatrix} 1 & 1 & 1 & 1 & 1 & 1 & 1 & 1 \\ 1 & 1 & 1 & 1 & -1 & -1 & -1 & -1 \\ 1 & 1 & -1 & -1 & 1 & 1 & -1 & -1 \\ 1 & 1 & -1 & -1 & -1 & -1 & 1 & 1 \\ 1 & -1 & 1 & -1 & 1 & -1 & 1 & -1 \\ 1 & -1 & 1 & -1 & -1 & 1 & -1 & 1 \\ 1 & -1 & -1 & 1 & 1 & -1 & -1 & 1 \\ 1 & -1 & -1 & 1 & -1 & 1 & 1 & -1 \end{bmatrix} \quad [21]$$

As in the case of Fourier encoding, each spin is excited by all of the encoding functions. The Hadamard encoding functions differ from the Fourier encoding functions only in their phase; thus, the scaling of the RF pulses is the same as in the Fourier encoding method. With the variable-flip-angle technique, the same flip angle scaling matrix $\overline{\overline{\Lambda}}$ that is used for normalized Fourier encoding can also be used for Hadamard encoding.

*2.3.3. Direct encoding.* The direct encoding matrix is the identity matrix. In direct encoding, there is no explicit "encoding" and therefore no reconstruction is required. Thus the encoding functions are the same as the spatially localized basis defined in Eq. [1]. For direct encoding, because each pixel location within an individual line is excited one time only, a flip angle of 90° can be used for each excitation.

*2.3.4. Wavelet encoding.* Unlike the Fourier transform, where the signal is modulated with different frequencies, the wavelet transform encodes the signal in both the frequency and the spatial domains. With this additional degree of freedom, wavelet encoding has been shown to be suitable for multiresolution adaptive imaging strategies (*1*). In a true wavelet transform, each wavelet basis is associated with a particular point-spread function. With the introduction of the digital wavelet encoding concept (*8*), the point-spread function is made independent of the wavelet basis used. Thus, in this section, we focus only on the wavelet encoding matrix in terms of encoding basis normalization and RF pulse design.

*Standard wavelet encoding basis.* There are many wavelet encoding matrices (*7*). One well-known wavelet basis is represented by the Haar matrix $\overline{\overline{W}}$, shown in Eq. [22], for the case of $N = 8$.

$$\overline{\overline{W}} = \begin{bmatrix} 1 & 1 & 1 & 1 & 1 & 1 & 1 & 1 \\ 1 & 1 & 1 & 1 & -1 & -1 & -1 & -1 \\ 1 & 1 & -1 & -1 & 0 & 0 & 0 & 0 \\ 0 & 0 & 0 & 0 & 1 & 1 & -1 & -1 \\ 1 & -1 & 0 & 0 & 0 & 0 & 0 & 0 \\ 0 & 0 & 1 & -1 & 0 & 0 & 0 & 0 \\ 0 & 0 & 0 & 0 & 1 & -1 & 0 & 0 \\ 0 & 0 & 0 & 0 & 0 & 0 & 1 & -1 \end{bmatrix} \quad [22]$$

A complete wavelet multiresolution decomposition (*11*) includes functions that span the full FOV, as represented in Eq. [22] by the existence of some rows in $\overline{\overline{W}}$ in which all elements are nonzero. It is also possible to construct partial wavelet multiresolution decompositions where the FOV is subdivided into multiple sections. For example, Eq. [23] shows a two-section wavelet encoding matrix, $\overline{\overline{W}}_{(8,2)}$, that performs separate multiresolution decompositions within each of the two subsections of the FOV.

$$\overline{\overline{W}}_{(8,2)} = \begin{bmatrix} 1 & 1 & 1 & 1 & 0 & 0 & 0 & 0 \\ 0 & 0 & 0 & 0 & 1 & 1 & 1 & 1 \\ 1 & 1 & -1 & -1 & 0 & 0 & 0 & 0 \\ 0 & 0 & 0 & 0 & 1 & 1 & -1 & -1 \\ 1 & -1 & 0 & 0 & 0 & 0 & 0 & 0 \\ 0 & 0 & 0 & 0 & 1 & -1 & 0 & 0 \\ 0 & 0 & 1 & -1 & 0 & 0 & 0 & 0 \\ 0 & 0 & 0 & 0 & 0 & 0 & 1 & -1 \end{bmatrix} \quad [23]$$

subsection 0 subsection 1

Note that the odd rows of $\overline{\overline{W}}_{(8,2)}$ define basis functions that will encode only the left half of the FOV, and the even rows define basis functions that will encode only the right half of the FOV.

In general, the number of levels of resolution $Q$ for the wavelet matrix $\overline{\overline{W}}_{(M,K)}$ is

$$Q = \log_2(M/K) + 1, \quad [24]$$

where $M$ is number of pixels within the FOV, and $K$ is the number of separate subsections within the FOV, which can only assume a value of $2^i$, where $i$ is zero or a positive integer. For a complete wavelet multiresolution decomposition, $K = 1$ and $Q = \log_2 M + 1$. For example, if there are $M = 128$ pixels in the FOV, a complete wavelet encoding decomposes the FOV into eight separate levels of resolution. In the limiting case where the number of subsections is equal to the number of pixels ($M = K$), there is only one level of resolution. For this case, $\overline{\overline{W}}_{(M,M)}$ is the identity matrix that represents direct or line scan encoding. With such representation, multisection wavelet and direct encoding are integrated as one class of encoding scheme, which will ease the SNR analysis discussed below.

*Wavelet encoding basis normalization.* In both Eq. [22] and Eq. [23], the encoding bases are not normalized. The encoding functions represented by such matrices would be used for proton imaging to maximize SNR. As was analyzed previously, however, they are not appropriate for hyperpolarized noble gas imaging because they do not maximize SNR in hyperpolarized noble gas MRI. To normalize the wavelet encoding functions, the amplitude of each encoding function must be scaled by a factor that depends on the number of pixels excited by the function, so that

$$\overline{\overline{W}} \cdot \overline{\overline{W}}^{\mathrm{T}} = \bar{\bar{I}}, \quad [25]$$

where $\overline{\overline{W}}$ is the wavelet encoding matrix and $\bar{\bar{I}}$ is the identity matrix.

For example, the normalized matrices for Eqs. [22] and [23] are, respectively,

$$\overline{\overline{W}}^{\mathrm{norm}}_{(8,1)} = \begin{bmatrix} 1/\sqrt{8} & 1/\sqrt{8} & 1/\sqrt{8} & 1/\sqrt{8} & 1/\sqrt{8} & 1/\sqrt{8} & 1/\sqrt{8} & 1/\sqrt{8} \\ 1/\sqrt{8} & 1/\sqrt{8} & 1/\sqrt{8} & 1/\sqrt{8} & -1/\sqrt{8} & -1/\sqrt{8} & -1/\sqrt{8} & -1/\sqrt{8} \\ 1/2 & 1/2 & -1/2 & -1/2 & 0 & 0 & 0 & 0 \\ 0 & 0 & 0 & 0 & 1/2 & 1/2 & -1/2 & -1/2 \\ 1/\sqrt{2} & -1/\sqrt{2} & 0 & 0 & 0 & 0 & 0 & 0 \\ 0 & 0 & 1/\sqrt{2} & -1/\sqrt{2} & 0 & 0 & 0 & 0 \\ 0 & 0 & 0 & 0 & 1/\sqrt{2} & -1/\sqrt{2} & 0 & 0 \\ 0 & 0 & 0 & 0 & 0 & 0 & 1/\sqrt{2} & -1/\sqrt{2} \end{bmatrix} \quad [26]$$

and

$$\overline{\overline{W}}^{\mathrm{norm}}_{(8,2)} = \begin{bmatrix} \underbrace{\begin{matrix} 1/2 & 1/2 & 1/2 & 1/2 \\ 0 & 0 & 0 & 0 \\ 1/2 & 1/2 & -1/2 & -1/2 \\ 0 & 0 & 0 & 0 \\ 1/\sqrt{2} & -1/\sqrt{2} & 0 & 0 \\ 0 & 0 & 0 & 0 \\ 0 & 0 & 1/\sqrt{2} & -1/\sqrt{2} \\ 0 & 0 & 0 & 0 \end{matrix}}_{\text{subsection 0}} & \underbrace{\begin{matrix} 0 & 0 & 0 & 0 \\ 1/2 & 1/2 & 1/2 & 1/2 \\ 0 & 0 & 0 & 0 \\ 1/2 & 1/2 & -1/2 & -1/2 \\ 0 & 0 & 0 & 0 \\ 1/\sqrt{2} & -1/\sqrt{2} & 0 & 0 \\ 0 & 0 & 0 & 0 \\ 0 & 0 & 1/\sqrt{2} & -1/\sqrt{2} \end{matrix}}_{\text{subsection 1}} \end{bmatrix} \quad [27]$$

*Design of wavelet RF excitation pulses.* In the standard variable-flip-angle technique described in (*10*), the flip angle is varied so that the amount of transverse magnetization excited is the same for different encoding steps. This techniques can be directly used for Fourier or Hadamard encoding because all spins within the FOV are equally excited on each encoding step.

Calculating the appropriate flip angle for wavelet encoding using the variable-flip-angle technique is complicated because the signal amplitude is no longer constant for each excitation, and volume elements experience variable delay between excitations. The problem is illustrated by Fig. 4, which shows the Haar encoding functions arranged vertically according to the temporal order of excitations. First, the amplitude of the encoding function increases while fewer and fewer pixels are excited in each excitation. In addition, at pixel location $x_0$, spins are excited at time 0, $T$, $2T$, and $4T$. Although spins at locations $x_1$ are excited at the same times as $x_0$, the temporal pattern of excitation varies at other locations. When considering $T_1$ decay, to create the spin profile shown in Fig. 4, the flip angles of different pixels in each section have to be calculated separately.

In wavelet encoding, each pixel is excited $Q$ times, which is the

same as the total number of resolution levels defined in Eq. [24]. To fulfill the normalization requirement, the transverse magnetization after the $q$th excitation at each pixel location should be

$$S_q = \begin{cases} 1/\sqrt{N/K} & q = 1 \\ 1/\sqrt{N/(K \cdot 2^{q-2})} & q = 2, 3, \ldots, Q \end{cases}. \quad [28]$$

We also define $\tau_{qm}$ as the time between the $q$th and $(q+1)^{\text{th}}$ excitation at the pixel location $x_m$,

$$\tau_{qm} = \begin{cases} (2^{q-2} + \lfloor (m \bmod N/K)/2^{Q-q} \rfloor) \\ \quad \times K \cdot \text{TR} & 2 \le q \le Q-1, \\ K \cdot \text{TR} & q = 1 \end{cases} \quad [29]$$

where $0 \le m \le M-1$, TR is the repetition time of the sequence, and "$a$ mod $b$" represents "$a$ modulo $b$."

To directly calculate the flip angle of the spins in each pixel let us first calculate the residual longitudinal signal amplitude $Z_{nm}$ at pixel location $x_m$, immediately after the $q$th RF pulse,

$$Z_{qm} = \sqrt{(Z_{(q-1)m} e^{-\tau_{q-1}(x_m)/T_1(x_m)})^2 - S_q^2} \quad 1 \le q \le Q, \quad [30]$$

where $x_m = m\Delta x$ $(0 \le m \le M-1)$, $\Delta x$ is the pixel width, $M$ is the total number of pixels along the FOV, and $S_q$ and $\tau_{qm}$ are as defined in Eqs. [28] and [29]. To effectively utilize all of the hyperpolarized magnetization, no residual longitudinal signal should be left after the last RF pulse, i.e., $Z_{Qm} = 0$. Thus, according to Eq. [30],

$$Z_{qm} = \begin{cases} \sqrt{\sum_{j=q+1}^{Q} S_j^2 e^{2[\sum_{i=q}^{j-1} \tau_i(x_m)]/T_1(x_m)}} & 1 \le q \le Q-1 \\ 0 & q = Q \end{cases}. \quad [31]$$

Therefore, the flip angle of the $q$th RF excitation at pixel location $x_m$ for a normalized Haar wavelet encoding basis with $Q$ levels of resolution is

$$\theta_{qm} = \arctan\left(\frac{S_q}{Z_{qm}}\right) \quad [32]$$

$$= \begin{cases} \arctan(S_q/\sqrt{\sum_{j=q+1}^{Q} S_j^2 e^{2[\sum_{i=q}^{j-1} \tau_i(x_m)]/T_1(x_m)}}) & 1 \le q \le Q-1 \\ \pi/2 & q = Q \end{cases}, \quad [33]$$

where $S_q$ and $\tau_{qm}$ are as defined in Eqs. [28] and [29]. In the limiting case of direct encoding where $Q = 1$, because each pixel is excited only one time, every $\theta$ is set to $\pi/2$.

When the $T_1$ relaxation time is ignored, Eq. [33] can be simplified to

$$\theta_{qm} = \begin{cases} \arctan(S_q/\sqrt{\sum_{j=q+1}^{Q} S_j^2}) & 1 \le q \le Q-1 \\ \pi/2 & q = Q \end{cases}. \quad [34]$$

For example, when $T_1$ is ignored, the scaling matrices $\overline{\overline{\Lambda}}$ for the normalized complete and two-section wavelet encoding matrices described by Eqs. [26] and [27] are, respectively,

$$\overline{\overline{\Lambda}}_{(8,1)} = \begin{bmatrix} 59 & 59 & 59 & 59 & 59 & 59 & 59 & 59 \\ 63 & 63 & 63 & 63 & -63 & -63 & -63 & -63 \\ 71 & 71 & -71 & -71 & 0 & 0 & 0 & 0 \\ 0 & 0 & 0 & 0 & 71 & 71 & -71 & -71 \\ 127 & -127 & 0 & 0 & 0 & 0 & 0 & 0 \\ 0 & 0 & 127 & -127 & 0 & 0 & 0 & 0 \\ 0 & 0 & 0 & 0 & 127 & -127 & 0 & 0 \\ 0 & 0 & 0 & 0 & 0 & 0 & 127 & -127 \end{bmatrix} \quad [35]$$

and

$$\overline{\overline{\Lambda}}_{(8,2)} = \begin{bmatrix} \underbrace{\begin{matrix} 60 & 60 & 60 & 60 \\ 0 & 0 & 0 & 0 \\ 71 & 71 & -71 & -71 \\ 0 & 0 & 0 & 0 \\ 127 & -127 & 0 & 0 \\ 0 & 0 & 0 & 0 \\ 0 & 0 & 127 & -127 \\ 0 & 0 & 0 & 0 \end{matrix}}_{\text{subsection 0}} & \underbrace{\begin{matrix} 0 & 0 & 0 & 0 \\ 60 & 60 & 60 & 60 \\ 0 & 0 & 0 & 0 \\ 71 & 71 & -71 & -71 \\ 0 & 0 & 0 & 0 \\ 127 & -127 & 0 & 0 \\ 0 & 0 & 0 & 0 \\ 0 & 0 & 127 & -127 \end{matrix}}_{\text{subsection 1}} \end{bmatrix}. \quad [36]$$

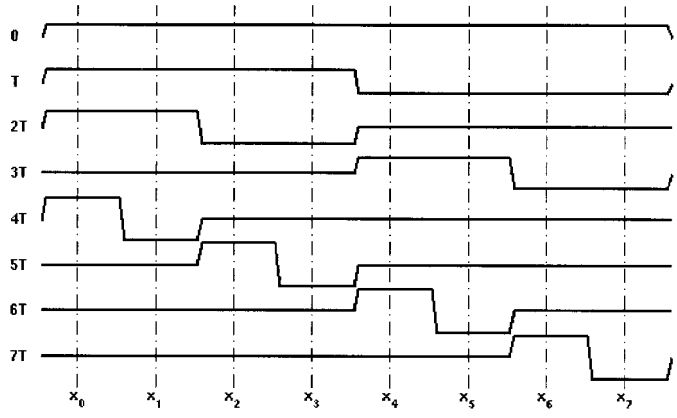


**FIG. 4.** Illustration of various encoding amplitudes and repetition times of spins in different volume elements using wavelet encoding matrix.

## 3. METHODS

### *3.1. Imaging System and Sequences*

We implemented normalized Fourier, Hadamard, wavelet, and direct encoding methods and conducted a series of experiments to compare the SNRs of these methods. All imaging was performed on a 1.5-T Signa imaging system (General Electric Medical Systems, Milwaukee, WI) with standard gradients. A doped water phantom imaged with a standard quadrature head coil was used for proton experiments for SNR comparisons. Images of a glass cell (7.5 cm long and 2 cm in diameter) containing hyperpolarized $^{129}$Xe were obtained at 17.7 MHz with a solenoid coil. Optical pumping of $^{129}$Xe gas was as described in (*10*). Computation of RF waveforms and image reconstruction was implemented with Matlab (The Mathworks, Inc., Natick, MA) on a separate SUN Sparc workstation (Sun Microsystems, Mountain View, CA).

A standard gradient echo sequence was used for normalized Fourier imaging. The variable-flip-angle technique described in (*10*) was applied to scale the RF pulses to excite normalized encoding profiles. In the Hadamard, wavelet, and direct encoding techniques, different spatial-selective RF pulses were used to excite the non-Fourier encoding functions along the *y* dimension. The *x* dimension was frequency encoded as usual. No slice selection was applied. Image resolution along the *y* dimension was 2.4 mm and along the *x* dimension it was 1.2 mm, for all of the encoding techniques.

The normalized encoding bases described in Section 2.3 were used for Fourier and Hadamard encoding. The normalized Haar wavelet basis $\overline{\overline{W}}_{(M,K)}$ (described in Section 2.3.4) was implemented with $M = 128$ and $K = 1, 2, 4, 8, 16, 32, 64$, and 128. When $K = 128$, the encoding matrix is just the identity matrix and the encoding represents a direct transform or line scan encoding. The point-spread function $\Phi(x)$ was a smoothed Haar box-shape function, the Fourier transform of a cosine windowed three-lobe sinc function. RF pulses were generated with Matlab, converted to Signa format, and transferred to the scanner.

For all imaging sequences, a TR of 50 ms and a TE of 25 ms were used. The dwell time of the RF encoding pulses was 30 $\mu$s, with 512 points defining each pulse shape, giving a total pulse duration of 15 ms. The image resolution was 128 (phase) by 256 (frequency) for all images.

In order to compare the hyperpolarization levels of noble gases for each image, a navigator excitation with a 1° flip angle was inserted at the beginning of the imaging sequences. With a 1° pulse, only 0.015% of the signal is depleted by the navigator echo; thus, there was no noticeable SNR decrease on the images.

### *3.2. Image Acquisition and Data Processing*

Proton images were acquired with the constant flip angle (CFA) technique for Fourier, Hadamard, wavelet, and direct encoding. A small flip angle of 7° was used for all CFA imaging in order to keep the peak RF amplitude within acceptable limits of the MR scanner for all Hadamard and wavelet excitations while still permitting SNR comparisons across all methods. Wavelet encoded images with the CFA technique were acquired at all possible levels of multiresolution decomposition, including the limiting case of direct encoding. The relative SNRs of the proton images were then compared for verification of the theoretical predictions (*2*).

Hyperpolarized $^{129}$Xe images were acquired with the variable-flip-angle technique for normalized Fourier, Hadamard, wavelet, and direct encoding. Wavelet encoded images with the variable-flip-angle technique were acquired at all levels of multiresolution decomposition, including the limiting case of direct encoding. Images were reconstructed with the inverse normalized encoding bases.

Image SNR was defined as the ratio of mean of the signal magnitude over the standard deviation of the noise. The mean signal value was measured in regions where there was a strong signal, while the noise value was measured in regions of no signal. After being scaled by the amplitude of the navigator signal, the SNRs obtained using all encoding methods were normalized with respect to the SNRs obtained using Fourier encoding and compared with theoretical predictions.

For comparison, we also developed a variable-flip-angle approach, in which the standard (nonnormalized) multisection wavelet encoding bases could be achieved for imaging hyperpolarized $^{129}$Xe. Image SNRs were both calculated theoretically and measured experimentally. The SNRs were normalized with respect to those using Fourier encoding for comparison.

## 4. RESULTS

### *4.1. Proton Imaging with Constant Flip Angle*

The relative SNRs of proton images (images are not shown) were compared with the theoretical results (Fig. 5a). The

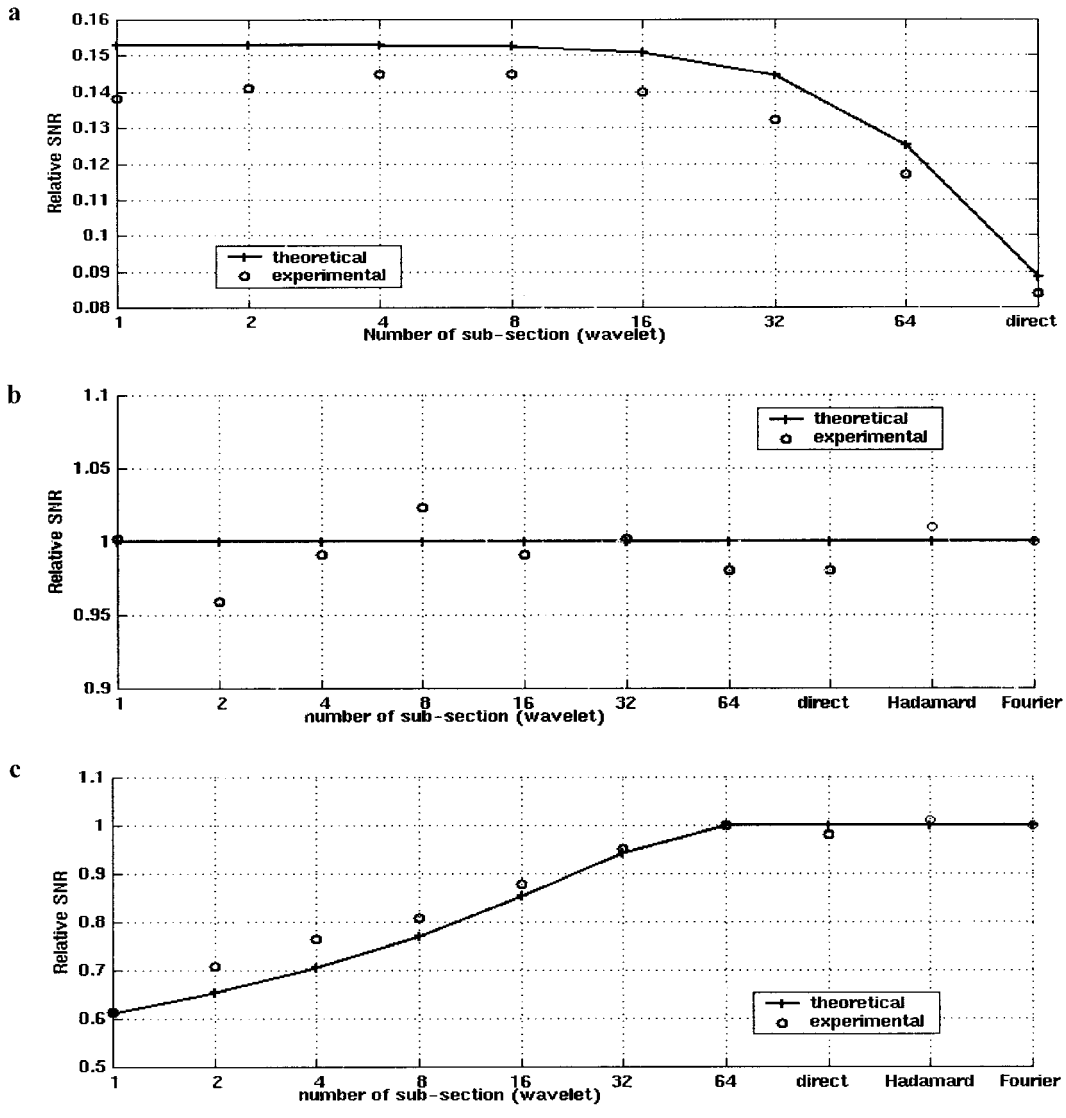


**FIG. 5.** Comparison of image SNRs of (a) proton, (b) $^{129}$Xe with normalized encoding bases, and (c) $^{129}$Xe with standard nonnormalized wavelet and normalized direct, Hadamard, and Fourier encoding. In (a), the relative SNR of Fourier and Hadamard encoding is 1.

symbol "o" represents experimental result, while the symbol "+" represents theoretical predication. The image SNR obtained using Fourier encoding is assumed to be 1, and other encoding methods are normalized to the SNR obtained using Fourier encoding. The SNR obtained using Hadamard encoding is the same as that obtained using Fourier encoding. Since a very small flip angle of 7° was used, the theoretical result was estimated with the assumption that magnetization was fully recovered between excitation. A close match between the theoretical predictions and experimental data can be seen. As shown in Fig. 5a, the wavelet and direct encoding methods applied for proton imaging produce much lower SNR than does Fourier or Hadamard encoding. The larger the number of subsections in multisection wavelet encoding, the smaller the SNR. Direct encoding (which represents the case of wavelet encoding with the maximum number of subsections) gives the worst SNR. The SNRs of the complete wavelet encoded image and the direct encoding image are only about 15.3 and 8.8%, respectively, of that of the Fourier or Hadamard encoded image when image resolution along the wavelet or phase encoding direction is 128. Note that the experimental result obtained for CFA proton wavelet encoding does not show the monotonic decrease in SNR with subsection number that is expected from the theoretical calculations (see Fig. 5a), probably because the longitudinal recovery of protons spins between excitations was not considered in the SNR estimations. We note that there is a consistent deviation of 5–10% between the theoretical and experimental results in Fig. 5a. This is probably due to the error in flip angle estimation.

### *4.2. Hyperpolarized $^{129}$Xe Imaging with Variable Flip Angle*

A comparison of theoretical and experimental SNRs with normalized Fourier, multisection wavelet, and direct encoding for hyperpolarized $^{129}$Xe imaging is shown in Fig. 5b. The "o" symbol represents experimental results and the "+" symbol represents theoretical SNRs. The normalized multisection wavelet and direct encoding methods, applied for hyperpolarized $^{129}$Xe imaging, produce SNRs that are the same as those of the normalized Fourier and Hadamard encoding, in stark contrast to the proton imaging case (Fig. 5a). The theoretical SNR predictions are corroborated by the experimental results. For comparison, an example of the relative image SNRs, obtained with standard wavelet encoding (nonnormalized) bases, is shown in Fig. 5c. As expected, image SNRs obtained using nonnormalized bases were lower than the SNRs obtained using the normalized encoding bases.

## 5. DISCUSSION

In this paper, we developed the theory for analyzing the image SNR of hyperpolarized noble gases, and conclude that *the image SNR for hyperpolarized noble gas imaging is maximized using any orthonormal encoding method.* On the basis of this finding, we derived algorithms to directly calculate the variable flip angles for RF encoding pulses so that normalized encoding bases could be achieved with the consideration of both $T_1$ relaxation and the depletion of hyperpolarized magnetization by the RF pulses.

We integrated multisection wavelet and direct encoding into one general scheme, with the same reconstruction matrix format. This method facilitates the understanding of the SNR relationship among the direct and the multisection wavelet encoding techniques. Excellent matches between the theoretical and experimental SNRs, for both proton and $^{129}$Xe imaging, have been demonstrated. These methods can be used to optimize imaging schemes with Fourier, Hadamard, wavelet, direct, or any other orthonormal encoding basis so that high-SNR images can be obtained with the most efficient utilization of hyperpolarization.

In wavelet and direct encoding, the SNR varies slightly with pixel location. Due to the longitudinal relaxation of noble gases, spins that are excited at a later time have a smaller signal than those that are excited earlier. In the direct encoding case, the last pixel is excited $(M - 1) * \mathrm{TR}$ after the first spins are excited (where $M$ is the number of pixels along the FOV). When the TR is much smaller than $T_1$, this effect is expected to be negligible.

When hyperpolarized noble gases are imaged, the hyperpolarized magnetization is $10^5$ times larger than the longitudinal magnetization at thermal Boltzmann equilibrium. Since the MR signal does not depend on the recovery of the thermal magnetization, long recycle delays are not needed. The absence of the detectable $^{129}$Xe or $^3$He signal at thermal equilibrium magnetization levels also eliminates a complication for wavelet encoding that exists in proton imaging: the uneven $T_1$ weighting across the FOV (*12*). In proton imaging, uneven weighting arises from the variation of the longitudinal recovery due to the variable TRs at different pixel locations. This problem is increased in proton wavelet imaging when the TR is short, complicating the application of wavelet encoding for many fast imaging techniques. By contrast, in hyperpolarized noble gas imaging the situation actually improves with shorter TR. When TR is much less than $T_1$, the uneven weighting effect is totally eliminated.

In our experiments, no slice selection was applied. To achieve slice selection, a 180° pulse that refocuses spins along a direction orthogonal to the initial excitation can be inserted into the non-Fourier encoding sequence. For multiple-shot imaging sequences, however, imperfect 180° RF pulses can destroy some of the stored longitudinal hyperpolarized magnetization (*13*), resulting in images with lower SNR. Alternatively, a 90° spatial-selective RF pulse can be used to eliminate all of the hyperpolarized magnetization outside of the slab of interest before the imaging sequence starts, and phase encoding can then be applied within the slab to obtain multiple slices. With this method, only a small amount of extra time is needed at the beginning of the imaging session to deplete the out-of-slab hyperpolarized magnetization.

Due to the nonlinear relationship between an RF pulse envelope and the spatial distribution of magnetization that it excites, image distortion can be introduced when a simple Fourier transform technique is used for RF pulse design at large flip angles. Since RF excitation is only used for slice selection, this is not an important issue for Fourier encoding. In non-Fourier encoding, however, the spatial distribution of excited magnetization itself participates in the encoding, so that the nonlinearity may introduce image artifacts. When the variable-flip-angle technique is applied to hyperpolarized noble gas imaging, in order to efficiently utilize all the hyperpolarization, flip angles as large as 90° pulse have to be applied. Therefore, it is expected that special RF pulse design techniques (*14–20*) will be needed to achieve accurate spatial profiles and artifact-free images. In our variable-flip-angle experiments, 90° pulses were used only on the last excitation for wavelet, Hadamard, and Fourier encoding and on all encoding steps for direct encoding. Using these encoding methods, even though the RF pulses were designed by simple Fourier transformation, no noticeable distortion was seen in the images. For the direct imaging technique, because all the pixels across the FOV are excited with the same profile, slight profile distortions will not introduce noticeable artifacts. In other encoding methods, a 90° pulse was used for only the high-resolution profiles. Owing to the small signal associated with these encoding steps, it is unlikely that there will be any noticeable artifact.

In our SNR analysis, we assumed that spins stay within each pixel boundary during the excitation. The analysis will be affected by motion of the spins. One source of motion is

diffusion. For example, our 3-atm Xe cell phantom has a diffusion constant of $D = 0.02$ cm$^2$/s (*21*). During the 15-ms RF pulse application ($t_{RF}$), $^{129}$Xe atoms will diffuse $\delta X_{diff} = (2Dt_{RF})^{1/2} = 0.2$ mm (*9*). Thus, when pixel size is small, especially comparable to the diffusion length, the SNR analysis and the RF generation methods may not hold. When pixel size is large or when the duration of the RF pulse is short, however, the effect of diffusion can be ignored for the SNR analysis.

A gas circulation system (*22*) can provide a continuous flow of hyperpolarized noble gases (*23*). With the replenishing of hyperpolarized gases, MR signal levels can be expected to increase considerably. This improved MR signal can significantly help in many hyperpolarized noble gas NMR spectroscopy and MRI applications (*24*). Image SNR calculation with continuous flow is complicated because there is flow-in of newly hyperpolarized gas and flow-out of depolarized gas. The hyperpolarization level of each pixel relies on the initial magnetization, the RF pulse flip angles applied, and the flow velocity and direction. If the flow is fast enough, the hyperpolarized magnetization at each pixel in the FOV is fully replenished with newly polarized gas between excitations. In this case, image SNR comparison is the same as that described in Scenario I. Further investigations will focus on the modeling of flow with the consideration of flow velocity, direction, and their relationship with the utilization of hyperpolarized magnetization during imaging.

In summary, imaging of a hyperpolarized $^{129}$Xe cell using normalized Fourier, Hadamard, wavelet, and direct encoding was implemented and the relative SNRs were measured and compared across the various encoding methods. With the SNR of Fourier encoding as a reference, the relative SNRs obtained using wavelet and direct encoding were shown to increase dramatically from 0.153 and 0.088, respectively, in proton imaging to 1.0 for hyperpolarized gas imaging where all orthonormal encoding methods have identical SNR. Even for the case of TR $\leq T_1$ (Scenario II), there is still a significant SNR difference for proton imaging between Fourier encoding and spatially localized encoding methods such as direct encoding. The SNR equivalence of all orthonormal encoding methods in hyperpolarized noble gas imaging is of striking significance, because it opens the door for new applications of non-Fourier encoding methods. In particular, the spatial localization feature of some non-Fourier encoding methods make them suitable for dynamically adaptive imaging.

## APPENDIX

THEOREM 1. *For a group of nonnegative real numbers* $a_1, a_2, \cdots, a_n$, *if* $a_1 + a_2 + \cdots + a_n = C$, *where C is a constant larger or equal to zero and n is any integer number which is larger or equal to* 2. $S_n = 1/a_1 + 1/a_2 + \cdots + 1/a_n$ *will be minimized only if* $a_1 = a_2 = \cdots = a_n = C/n$.

*Proof.* We will use the induction method to prove this theorem.

1. Let's first prove the theorem for the case of $n = 2$. When $n = 2$, $a_1 + a_2 = C$. Thus,

$$S_2 = \frac{1}{a_1} + \frac{1}{a_2} = \frac{1}{a_1} + \frac{1}{C - a_1} = \frac{C}{a_1(C - a_1)}. \quad [37]$$

Because the coefficient of $a_1^2$ in the quadruple function $a_1(C - a_1)$ is $-1$, function $a_1(C - a_1)$ has a maximal value. Since $C$ is not negative, $S_2$ has a minimal value. When the derivative of $S_2$ is 0, $S_2$ is minimized. Based on Eq. [37],

$$\frac{dS_2}{da_1} = d\left(\frac{C}{a_1(C - a_1)}\right)/da_1 \quad [38]$$

$$= \frac{C(2a_1 - C)}{a_1^2(C - a_1)^2}. \quad [39]$$

To solve $dS_2/da_1 = 0$, we get $a_1 = a_2 = C/2$, when $S_2$ is minimized.

2. Let's then prove that if the theorem is true for the case of $n = N - 1$, it is true for the case of $n = N$, where $N$ is an integer and is larger than 2. When $n = N$ and $a_1 + a_2 + \cdots + a_N = C$, we want to minimize $S_N = 1/a_1 + 1/a_2 + \cdots + 1/a_N$. For ANY fixed $a_N$, to minimize $S_N = S_{N-1} + 1/a_N$ is equivalent to minimize $S_{N-1}$. Since the theorem is true for $n = N - 1$, for any $a_N$, $S_{N-1}$ will be minimized only if $a_1 = a_2 = \cdots = a_{N-1} = (C - a_N)/(N - 1)$. Therefore,

$$S_N = \frac{1}{a_1} + \frac{1}{a_2} + \cdots + \frac{1}{a_N} = \frac{(N - 1)^2}{(C - a_N)} + \frac{1}{a_N}. \quad [40]$$

Similar to the proof in [1], $S_N$ has a minimum value. To minimize $S_N$, according to Eq. [40], we should set the derivative of $S_N$ to be 0,

$$d\left(\frac{(N - 1)^2}{(C - a_N)} + \frac{1}{a_N}\right)/da_N = 0. \quad [41]$$

The solution to Eq. [41] is $a_N = C/N$. Therefore, when $a_1 = a_2 = \cdots = a_{N-1} = a_N = C/N$, $S_N$ is minimized.

3. According to [1] and [2] and based on the induction theory, for any $n$ with $a_1 + a_2 + \cdots + a_n = C$, only if $a_1 = a_2 = \cdots = a_n = C/n$, the summation $S_N = 1/a_1 + 1/a_2 + \cdots + 1/a_N$ is minimized and equals $n^2/C$.

## ACKNOWLEDGMENTS

This work was performed with support from the Whitaker Foundation (RG-94-0172, TF-97-0002, and RG-95-0192), NIH (R29-CA70314, R01-HL57563), NSF (BES-9617342), and NASA (NAG9-1041).

## REFERENCES


1. L. P. Panych and F. A. Jolesz, A dynamically adaptive imaging algorithm for wavelet encoded MRI, *Magn. Reson. Med.* **32,** 738–748 (1994).
2. L. P. Panych, Theoretical comparison of Fourier and wavelet encoding in magnetic resonance imaging, *IEEE Trans. Med. Imaging* **15**(2), 141–153 (1996).
3. M. S. Albert, G. D. Cates, B. Driehuys, W. Happer, B. Saam, C. S. Springer, Jr., and A. Wishnia, Biological magnetic resonance imaging using laser-polarized $^{129}$Xe, *Nature* **370,** 199–201 (1994).
4. L. P. Panych, G. P. Zientara, P. Saiviroonporn, S-S. Yoo, and F. A. Jolesz, Digital wavelet encoded MRI—A new wavelet encoding methodology. *J. Magn. Reson. Imaging* **8,** 1135–1144 (1998).
5. L. P. Panych, G. P. Zientara, and F. A. Jolesz, MR image encoding by spatially selective RF excitation: An analysis using linear system models. *J. Imag. Syst. Technol.* **10,** 143–150 (1999).
6. G. Battle, Cardinal spline interpolation and the block spin construction of wavelets. *in* "Wavelets: A Tutorial in Theory and Applications" (C. K. Chui, Ed.), Vol. 2, pp. 73–90, Academic Press, San Diego, 1992.
7. C. K. Chui, "An Introduction to Wavelets," Academic Press, San Diego, 1992.
8. L. P. Panych, P. Saiviroonporn, G. P. Zientara, and F. A. Jolesz, Digital wavelet encoded MRI—A new wavelet encoding methodology, *in* "Proceedings of the ISMRM," p. 1989, 1997.
9. P. T. Callaghan, "Principles of Nuclear Magnetic Resonance Microscopy," Clarendon, Oxford, 1991.
10. L. Zhao, R. Mulkern, C. H. Tseng, D. W. Williamson, S. Patz, R. Kraft, R. L. Walsworth, F. A. Jolesz, and M. S. Albert, Gradient-echo imaging considerations for hyperpolarized $^{129}$Xe MR. *J. Magn. Reson. B* **113,** 179–183 (1996).
11. S. G. Mallat, A theory for multiresolution signal decomposition: The wavelet representation. *IEEE Trans. Pattern Anal. Mach. Intell.* **11,** 674–693 (1989).
12. P. Saiviroonporn, "Adaptive Non-Fourier Spatial Encoding for Dynamic MRI," Ph.D. thesis, Boston Univ., Boston, MA, 1997.
13. L. Zhao and M. S. Albert, Biomedical imaging applications of hyperpolarized noble gases: Pulse sequence considerations. *Nucl. Instrum. Methods Phys. Res. Sect. A* **402,** 454–460 (1998).
14. W. E. Kyriakos and L. P. Panych, Implementation of wavelet encoded MRI with large flip-angle RF pulses, *in* "Proceedings of the ISMRM," p. 1990, 1997.
15. D. I. Hoult, The solution of the Bloch equations in the presence of a varying B1 field—An approach to selective pulse analysis. *J. Magn. Reson.* **35,** 69–86 (1979).
16. M. R. Smith, RF pulse shapes for selective excitation in NMR imaging, *IEEE Trans. Med. Imaging MI* **4,** 79–83 (1985).
17. S. Conolly, D. Nishimura, and A. Macovski, Optimal control solutions to the magnetic resonance selective excitation problem. *IEEE Trans. Med. Imaging MI* **5,** 106–115 (1986).
18. J. Pauly, D. Nishimura, and A. Macovski, A linear class of large-flip-angle selective excitation pulses. *J. Magn. Reson.* **82,** 571–587 (1989).
19. J. Pauly, D. Nishimura, and A. Macovski, A *k*-space analysis of small-tip-angle excitation. *J. Magn. Reson.* **81,** 43–56 (1989).
20. J. Pauly, D. Nishimura, and A. Macovski, Parameter relations for the Shinnar–Le Roux selective excitation pulse design algorithm. *IEEE Trans. Med. Imaging* **10,** 53–65 (1991).
21. L. Zhao, R. Mulkern, A. Venkatesh, H. Gubbjartsson, F. A. Jolesz, and M. S. Albert, Hyperpolarized $^{129}$Xe $T_2$ and diffusion measurement for fast spin-echo MRI, *in* "Proceedings of the ISMRM, Sixth Scientific Meeting and Exhibition," p. 451, 1998.
22. M. Haake, A. Pine, J. A. Reimer, and R. Seydoux, Surface-enhanced NMR using continuous-flow laser-polarized xenon. *J. Am. Chem. Soc.* **119**(48), 11711–11712 (1997).
23. E. Brunner, M. Haake, L. Kaiser, A. Pines, and J. A. Reimer, Gas flow MRI using circulating laser-polarized $^{129}$Xe. *J. Magn. Reson.* **138,** 155–159 (1999).
24. E. Brunner, Applications of laser-polarized $^{129}$Xe under continuous flow, *Magn. Reson. Chem.* **37,** S14–S22 (1999).